T Odstrcil et al.

The physics of W transport illuminated by recent progress in W density diagnostics at ASDEX Upgrade

The physics of W transport illuminated by recent progress in W density diagnostics at ASDEX Upgrade

T. Odstrcil[1,2]**, T. Pütterich**[1]**, C. Angioni**[1]**, R. Bilato**[1]**,
A. Gude**[1]**, M. Odstrcil**[3]**, M. Sertoli**[1,4]**,
ASDEX Upgrade Team and the EUROfusion MST1 team‡**

[1]Max-Planck-Institut für Plasmaphysik, D-85748 Garching, Germany
[2]Physik-Department E28, Technische Universität München, Garching, Germany
[3]Paul Scherrer Institut, CH-5232 Villigen PSI, Switzerland
[4]CCFE, Culham Science Centre, Abingdon, Oxon, OX14 3DB, UK

E-mail: `todstrci@ipp.mpg.de`

Abstract.
Due to the high mass and charge of the heavy ions, centrifugal and electrostatic forces cause a significant variation in their poloidal density. The impact of these forces on the poloidal density profile of tungsten was investigated utilizing the detailed two-dimensional SXR emissivity profiles from the ASDEX Upgrade tokamak. The perturbation in the electrostatic potential generated by magnetic trapping of the non-thermal ions from neutral beam injection was found to be responsible for significant changes in the poloidal asymmetry. An excellent match with the results of fast particle modeling was obtained, validating the model for the poloidal fast particle distribution. Additionally, an enhancement of the neoclassical transport due to an outboard side impurity localization was measured in the experiment using a perturbation in the tungsten flux caused by regular sawtooth activity. A qualitative match with neoclassical modeling was found, demonstrating the possibility of minimising neoclassical transport by an optimization of the poloidal asymmetry profile of the impurity.

PACS numbers: 52.25.Vy, 52.25.Xz,52.25.Fi,52.55.Fa,52.70.La

‡ Meyer et al, Overview of progress in European Medium Sized Tokamaks towards an integrated plasma-edge/wall solution, accepted for publication in Nuclear Fusion

1. Introduction

High melting temperature, low erosion rate and low retention of tritium make tungsten a promising candidate for the plasma facing components (PFC) in future fusion devices. Today, several fusion experiments investigate tungsten as a wall material such as ASDEX Upgrade (AUG) with a full W wall. Also, JET features W as a PFC in the divertor and Be at the main chamber wall resembling the wall mix planned for ITER. Nevertheless, if W is transported into the main plasma, strong radiation of the partially stripped W ions can significantly deteriorate the fusion gain [1]. This danger is facilitated by the scaling of the inward neoclassical convection with impurity charge Z, which may lead to central impurity accumulation and possibly to a subsequent radiation collapse of the plasma [2]. A deeper understanding and experimental validation of the high-Z impurity transport is, therefore, essential for the prediction of the stability and the performance of fusion reactors.

The large mass m_z and the charge Z of W ions make them susceptible to centrifugal and electrostatic forces, resulting in a poloidal variation of their density, i.e. asymmetry δ, quantified as the normalized cosine component of the poloidal impurity profile. The importance of the inertia in the parallel force balance was noticed already in references [3–5] and discussed in detail in paper [6]. The centrifugal force (CF), counteracted by a pressure and electrostatic force from other ions, increases the impurity density at the low-field side (LFS) of the magnetic flux surfaces. The electrostatic force is also generated by non-thermal ions with anisotropic pressure. A large fraction of these fast ions are magnetically trapped ions on the LFS which perturbs the poloidal electric potential and pushes the impurities towards the high field side (HFS). This is illustrated by a tomographic reconstruction of the SXR emissivity in neutral beam injection (NBI) only 1a and with additional ion cyclotron range of frequencies (ICRF) heating 1b, clearly demonstrating a LFS and HFS localization of the tungsten radiation.

This effect was first predicted for the fast ions from the NBI in [7] and later for fast ions produced by ICRF heating [8], which were indirectly observed for on Ni impurity in the JET tokamak [9] and recently in the Alcator C-Mod tokamak [10].

Furthermore, at the beginning of fusion research, it was already pointed out that the particle transport is not constant on the flux surfaces and thus a poloidal
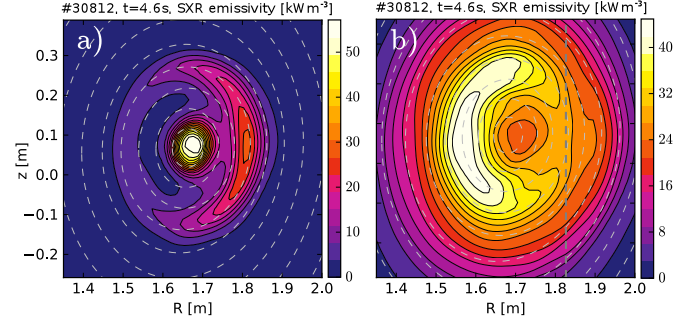

Figure 1. Tomographic reconstruction of the SXR emissivity in AUG discharge 30812 at a) 4.4 s with 2.5 MW of NBI heating only and b) with additional 4.3 MW of ICRF, vertical dashed line indicate IC resonance.

impurity asymmetry in density or sources can significantly affect the impurity flux [3–5, 11–13]. The enhancement of the neoclassical impurity fluxes was examined for bulk and impurity species in the banana regime [4, 14] and the Pfirsch-Schlüter (PS) regime [15, 16]. Additionally, the combination of the banana regime for the bulk ions and the PS regime for the impurity ions [17, 18] was investigated. The latter approach is the closest to the conditions of heavy impurities in the core of a AUG plasmas. These models predicted an increase of an order of magnitude of the neoclassical impurity flux for a Mach number $M_z = \omega_\varphi R / \sqrt{2T_z/m_z}$ above one, where ω_φ is the toroidal angular velocity, R the major radius of the tokamak and T_z the impurity temperature.

On the other hand, experimental validations are scarce. Plasma rotation scans performed on TFTR [19,20], MAST [21] and JT-60U [22–24] tokamaks revealed a strong dependence of the core impurity density on the magnitude and direction of the rotation velocity. However, a connection to the poloidal asymmetries has not been discussed. Asymmetries were considered in recent studies of the tungsten transport in hybrid discharges in JET [25–27] and AUG [27], where the closest match with the experimental impurity profiles was achieved when the centrifugal effects were included in the modeling by the drift-kinetic code NEO [16, 28, 29] and gyro-kinetic code GKW [30, 31].

In this work, a brief overview of the parallel transport theory is provided in section 2 and the effect of the poloidal asymmetries on the radial transport is modeled by the NEO code in section 3. The presence of tungsten asymmetries driven by fast NBI ions is demonstrated using a tomographic inversion of soft X-ray (SXR) profiles

dominated by W emission and compared with the parallel transport theory (section 4). In section 5, the impact of the centrifugal and electrostatic driven asymmetries on the radial impurity transport are investigated experimentally using sawtooth perturbations acting on the intrinsic W density.

2. Parallel force balance

Often it is assumed that the partial pressure p_α of plasma species α is constant along the magnetic field lines because the parallel transport is fast enough to suppress any deviation. However, in the presence of poloidally directed forces acting upon particles a significant poloidal variation can arise. The poloidal density profile is determined by force balance equations which are derived in the lowest order of the gyroradius expansion for the Maxwellian species [32]:

$$\nabla p_\alpha + \nabla \cdot \pi_\alpha - n_\alpha m_\alpha (\mathbf{u}_\alpha \cdot \nabla)\mathbf{u}_\alpha$$
$$+ Z_\alpha n_\alpha \nabla \Phi + Z_\alpha n_\alpha (\mathbf{u}_\alpha \times \mathbf{B}) = \mathbf{F}_\alpha \qquad (1)$$

where $\mathbf{u}_\alpha$ is mean flow of the species, π_α is the viscosity tensor, Φ the electric potential and F_α is a sum of all friction forces. In order to treat the parallel transport independently of cross-field transport, the parallel equilibrium must be established promptly with respect to the cross-field equilibration timescale $\tau_{\perp,\alpha}$, i.e. $\tau_{\perp,\alpha} \gg \tau_{\parallel,\alpha}$. Such an assumption is well fulfilled in the core of AUG where $\tau_{\perp,\alpha}/\tau_{\parallel,\alpha} \sim 10^3$ and the cross-field transport will act on a stationary, yet still asymmetric, impurity profile. However, at the plasma edge, the thermal velocity of heavy impurity ions like tungsten is low and this assumption is violated. In this case, the parallel and cross-field transport must be treated simultaneously [33, 34]. The viscosity tensor in equation (1) is negligible compared to the other terms and the inertia term is dominated by the toroidal contribution [35]. The projection of equation (1) along the field lines yields the parallel force balance equation

$$T_\alpha \nabla_\parallel n_\alpha + e Z_\alpha n_\alpha \nabla_\parallel \Phi + \frac{1}{2} m_\alpha \nabla_\parallel u_\alpha^2 = F_{\alpha\parallel}. \qquad (2)$$

The poloidal asymmetry driven by the friction force $F_{\alpha\parallel}$ is relevant only for the plasma edge, where large gradients in ion temperature and density together with high collisionality cause strong ion impurity friction [17] while the magnitude of the friction in the core of tokamak plasma is negligible [36]. The pressure term is dominant for light impurities, suppressing any poloidal variation, while the heavy impurities are in addition affected by the inertial and the electrostatic term. The coupled differential equations (2) under the assumption of the charge quasineutrality $\sum_\alpha n_\alpha Z_\alpha = 0$ provide enough constraints to determine the poloidal variation of the electric potential $\Phi(\theta)$ and the density profiles $n_\alpha(\theta)$ for all plasma species. Integrating the parallel force balance equations, the poloidal variation of density has the form

$$\frac{n_\alpha}{n_\alpha^*} = \exp\left[-\frac{eZ_\alpha(\tilde{\Phi})}{T_\alpha} + \frac{m\omega^2}{2T_\alpha}(R^2 - R^{*2}) \right], \qquad (3)$$

where the asterisk denotes the value at the outer midplane, i.e. LFS, and $\tilde{\Phi} \equiv \Phi - \Phi^*$ represents a perturbation in the electrostatic potential. Inserting the density profile (3) into the quasineutrality relation and expanding the exponential function, results in the following equation for the electrostatic potential

$$\frac{e\tilde{\Phi}}{T_e} = \frac{T_i}{T_i + Z_{\text{eff}} T_e} \frac{m_{\text{eff}} \omega_\phi^2}{T_i} \left(R^2 - R^{*2}\right). \qquad (4)$$

The effective mass m_{eff} can be estimated as $m_{\text{eff}} \approx m_i Z_{\text{eff}}$ for fully stripped light impurities in deuterium plasma. After substituting (4) back to (3) an approximation of the poloidal variation of heavy impurity density is found

$$\ln\left(\frac{n_z}{n_z^*}\right) \approx \frac{m_z \omega_\phi^2}{2T_i} \left(1 - \frac{Z_z}{m_z} \frac{m_{\text{eff}} T_e}{T_i + Z_{\text{eff}} T_e}\right)(R^2 - R^{*2}), \quad (5)$$

where the subscript z refers to the heavy impurity in the trace limit, while the subscript i corresponds to the bulk ions and e to electrons. The presence of other impurities or an increased mass of bulk ions reduces the heavy ion asymmetry, because their centrifugal asymmetry increases the perturbation in Φ, which counteracts the centrifugal force acting on the heavy ions.

Up to now, only the Maxwellian species were considered. However, fast ions produced by various heating sources are far from the thermal equilibrium. The gyro-orbits of the fast particles are determined by the constants of motion: energy $\mathcal{E} = mv^2/2$, magnetic moment $\mu = mv_\perp^2/2B$ and canonical angular momentum $\mathcal{P}_\varphi = mRv_\varphi + q\psi$, where ψ is poloidal magnetic flux. Using the zero orbit width approximation, i.e. particles do not deviate from flux surface with radial coordinate r, the density profile n_f of a species with a distribution function $f(r, \mu, \mathcal{E})$ is expressed as

$$n_f(r, B) = 4\pi \int_0^\infty \mathrm{d}\mathcal{E} \int_0^{\mathcal{E}/B} \mathrm{d}\mu \frac{B}{v_\parallel} f(r, \mu, \mathcal{E}),. \qquad (6)$$

where the magnetic field $B(\theta)$ represents the poloidal coordinate and the parallel velocity is $v_\parallel = \sqrt{2(\mathcal{E} - \mu B)}$. If the particle distribution fulfills $\frac{\partial f}{\partial \mu} = 0$, like a a Maxwellian distribution, the density n_f will be independent of the poloidal coordinate. A more convenient form of formula (6) can be derived after a coordinate transformation to the pitch $\xi \equiv v_\parallel/v$ and energy coordinates

$$n_f(r, B) = \frac{1}{2} \int_{-1}^1 \mathrm{d}\xi \int_0^\infty \mathrm{d}\mathcal{E} f^*(\xi^*(r, \xi, B), \mathcal{E}) \qquad (7)$$

and the LFS value of the pitch ξ is calculated from the conservation laws of $\mathcal{E}$ and μ:

$$\xi^*(\xi, B) = \text{sgn}(\xi)\sqrt{1 - \frac{B^*}{B}(1 - \xi^2)}. \qquad (8)$$

Note, that due to the high energy and low charge of the fast ions, the effect of the self-generated perturbation in the potential Φ is negligible. If we express $\tilde{\Phi}$ via the Boltzmann relation, use quasineutrality and insert it back into (3), a final expression for the poloidal profile of heavy ions in the presence of the non-Maxwellian species is found

$$\ln\left(\frac{n_z}{n_z^*}\right) \approx -\frac{n_f - n_f^*}{n_e}\frac{Z_z Z_f T_e}{T_i + Z_{\text{eff}} T_e} +$$
$$+ \frac{m_z \omega_\varphi^2}{2 T_i}\left(1 - \frac{Z_z m_i}{m_z}\frac{Z_{\text{eff}} T_e}{T_i + Z_{\text{eff}} T_e}\right)(R^2 - R^{*2}). \quad (9)$$

This approximation provides an excellent match with the direct solution of the parallel force balance [37], if the heavy impurity is a trace and other species yield small centrifugal asymmetries. The fast particles fraction asymmetry $(n_f - n_f^*)/n_e$ produced by ICRF and NBI has a typical value of 10^{-2} at AUG, with negligible impact on the bulk ions and low-Z impurities. However, for heavy impurities like tungsten with an average ionization state of about 45 at $T_e = 5\,\text{keV}$, a clearly observable asymmetry may be present. While the centrifugal force pushes impurities always towards the LFS, the fast particles affect heavy ion asymmetry in either direction depending on their distribution function. Passing fast ions accumulate on the HFS, pushing heavy ions towards the LFS. If the trapped fast ions dominate, the electrostatic force will counteract the centrifugal force and the heavy ions will concentrate at the HFS.

The key element of the accurate asymmetry modeling is the poloidal distribution of the fast particles. In order to include the orbit and centrifugal effects on the fast ions, a modeling code following the guiding-center orbits is necessary. For this purpose, we have applied the NUBEAM code [38] which is part of the TRANSP suite of codes. NUBEAM provides the 4D distribution functions of fast NBI ions on a $(\rho, \theta, \xi, \mathcal{E})$ grid, where ρ and θ is radial and angular coordinate. The fast particle density is then obtained by a trivial integration over the ξ, $\mathcal{E}$ coordinates. A model for the fast ions accelerated by ICRF was proposed in [39] and explicit formulas for the poloidal variation of density and temperature, neglecting the finite orbit effects, were presented in [37, 40].

In conclusion, the knowledge of the fast particle distribution and the centrifugal force enables the evaluation of the poloidal profile of heavy ions and vice versa, the precise measurement of the poloidal asymmetry allows to infer valuable information about the fast particle distribution [41].

3. Influence of poloidal asymmetries on impurity transport

The investigation presented in this paper focuses primarily on the neoclassical transport. The neoclassical flow of heavy impurities in the plasma core is dominated by the PS contribution which reverses its direction between the LFS and the HFS of the plasma due to a change in the sign of the parallel PS current and the parallel ion-impurity friction [18]. Since both, the LFS and the HFS contributions to the PS flow have similar magnitude, a small imbalance of the impurity density leads to a large change of the radial neoclassical flux. The neoclassical transport was modeled using the NEO code, which is presently the only neoclassical code including asymmetry effects [16]. Moreover, in contrast to the analytical approximations provided in [17, 18], NEO is valid for arbitrary collisionality and plasma geometry.

In order to analyze separately various contributions to the impurity transport, the neoclassical impurity flux Γ_z modeled by NEO was decomposed in the following way:

$$\frac{R\langle \mathbf{\Gamma_z} \cdot \nabla r\rangle}{\langle n_z\rangle} = D_z\left(\frac{R}{L_{\langle n_z\rangle}} + Z_z P_n \frac{R}{L_{n_i}} + Z_z P_T \frac{R}{L_{T_i}}\right) \quad (10)$$

where the impurity diffusion coefficient D_z is defined with respect to the gradient of flux surface average impurity density $\langle n_z\rangle$, and peaking factors P_n and P_T determine the impact of the normalized gradient lengths of ion density R/L_{n_i} and temperature R/L_{T_i} on the convective flow.

The impact of a poloidal asymmetry on D_z, P_T and P_n was examined by a poloidal asymmetry scan with the NEO code (in figure 2) for tungsten ions in the ionization state $Z = 45$. In NEO, the impurity asymmetry is directly computed ensuring quasineutrality, thereby a variation of the asymmetry was realized by including an anisotropic fast particle population in the model to push impurity ions towards HFS, and than varying the counteracting centrifugal force via the Mach number. The magnetic equilibrium and the kinetic profiles were adopted from the AUG discharge #30812 at $r/a = 0.3$ (local inverse aspect ration $\varepsilon = 0.1$), which features a normalized collisionality of bulk ions $\nu^* = 0.03$. The diffusion coefficient D_W in figure 2a grows almost linearly by an order of magnitude with respect to the minimum at slightly HFS asymmetry for $\delta/\varepsilon \approx -1$. The dashed line corresponds to the approximation in [18], which agrees with NEO only deep in the Pfirsch-Schlüter regime. This approximation shows a steeper parabolic dependence with a minimum at $\delta/\varepsilon = -2$.

The influence of the asymmetry on the stationary neoclassical normalized gradient of W density $R/L_{\langle n_z\rangle}$ is determined solely by the coefficients P_T and P_n depicted in figure 2b. While the P_n factor is almost unaffected, the P_T describing a ion temperature screening efficiency is enhanced by 50% at a large positive asymmetry and reduced by factor of two for $\delta/\varepsilon < 1$. The most
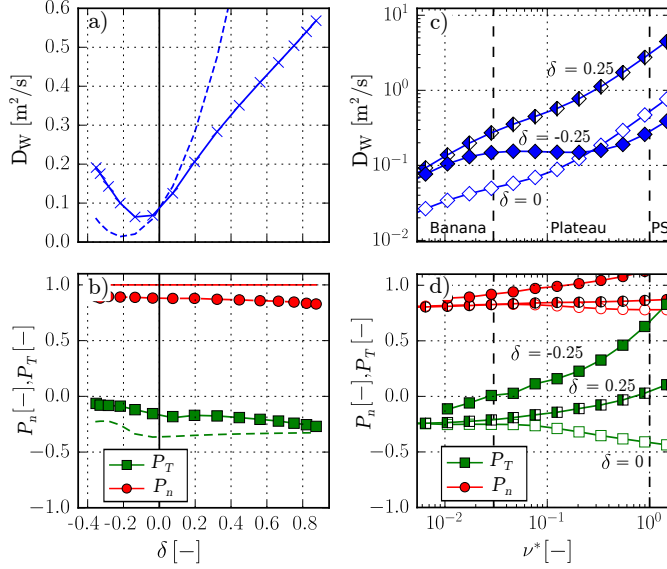
Figure 2. Neoclassical tungsten flux from the NEO code decomposed according to formula (10) scanned over *a-b* poloidal asymmetry and *c-d* normalized bulk ion collisionality ν^*, W collisionality is $Z_W^2 = 2045$ times higher. a) Full line corresponds to D_W from NEO at $r/a = 0.3$ ($\varepsilon = 0.1$), while the dashed line is an analytical model for the PS regime [18] normalized with respect to the $D_W(\delta = 0)$. b) Peaking factors P_T (green) and P_n (red) from NEO compared with analytical model for the PS regime (dashed lines). To avoid a non-physical singularity in the approximation at $\delta/\varepsilon = -2$, a classical diffusion was included.

favorable conditions to suppress the neoclassical impurity influx occurs for an asymmetry $-1 < \delta/\varepsilon < 0$, where the magnitude of the flux Γ_W given by D_W is small, while the T_i screening is still significant. The analytical approximation, denoted by the dashed line in figure 2, follows a similar trend as NEO. However, it is slightly shifted down.

At low collisionality ν^*, with W ions in the plateau regime, the minimum in D_W is close to a poloidally symmetric density. Then both, a positive and a negative asymmetry, increase the magnitude of the neoclassical D_W (figure 2c). When the collisionality is increased and thus the impurity collisionality moves deep into the PS regime, the minimum in D_W (figure 2a) shifts towards $\delta/\varepsilon = -2$ and the asymmetry dependence follows the approximation depicted in figure 2a. Ion temperature screening is described by P_T in figure 2d. At the symmetric case ($\delta = 0$), the P_T is doubled when the collisionality of the bulk ions changes from banana ($\nu^* < 0.03$) to PS regime ($\nu^* > 1$). However, in the presence of a moderate centrifugal asymmetry, the T_i screening is reduced. This effect was specifically identified in [26]. Moreover, P_T reverses its sign when the impurity collisionality moves into the PS regime. A negative asymmetry (i.e. impurities are localized on HFS) reduces the T_i screening even more and the direction of the convection is reversed already for a moderate bulk ion collisionality $\nu^* > 0.06$. In such a

case, both n_i and T_i gradients drive an inward impurity convection. These conditions may occur at the pedestal of the AUG plasmas, where a large HFS asymmetry of the light impurities has been observed [42].

4. Study of the poloidal asymmetry in NBI heated discharges

The poloidal distribution of the intrinsic tungsten density was measured employing the AUG SXR diagnostic [43]. This diagnostic provides eight pinhole cameras arranged in a poloidal plane of the plasma with a total of 208 lines of sight (LOS). A novel fast tomography code [44] was developed for the inversion of the measured line-integrated brightness, that provides high accuracy and resolution necessary for the investigation of the asymmetries and the impurity transport.

The in-out poloidal asymmetry δ is evaluated from the first cosine Fourier mode of the emissivity ε_{SXR} in the poloidal direction

$$\varepsilon_{\text{SXR}}(\rho, \theta) = \langle \varepsilon_{\text{SXR}} \rangle (1 + \delta(\rho) \cos \theta). \qquad (11)$$

The magnetic flux surfaces are determined by the kinetics constrained TRANSP equilibrium solver [45]. The accuracy of the magnetic equilibrium and of the SXR cameras alignment is essential for the measurements, because the error Δ_R in their mutual position results in asymmetry error $\Delta\delta$

$$\Delta\delta \approx \frac{\partial}{\partial r} \ln(\varepsilon_{\text{SXR}}(1 + \delta))\Delta_{\text{R}}. \qquad (12)$$

Due to the very steep tungsten SXR radiation profiles, the multiplication factor before Δ_{R} can reach values up to $20\,\text{m}^{-1}$. A sufficiently good accuracy is achieved using a self-consistent calibration and alignment of the diagnostic, as is described in [44]. It was applied to reduce systematical uncertainties in the geometry of the diagnostic, which were significantly degrading reconstruction accuracy.

Additionally, the SXR radiation asymmetry δ_{SXR} equals to the tungsten asymmetry δ_{W} only if the contributions of other plasma species to the SXR radiation are negligible. Since the light impurities have a negligible asymmetry a correction must be applied

$$\delta_{\text{SXR}} = \frac{\langle \varepsilon_W \rangle}{\langle \varepsilon_{\text{SXR}} \rangle} \delta_{\text{W}}, \qquad (13)$$

where ε_W is the W radiation and ε_{SXR} is the total SXR radiation of the plasma.

The poloidal asymmetries were investigated in the L-mode discharge #32566 with $2.5\,\text{MW}$ of NBI heating, a toroidal field of $B_T = 2.7\,\text{T}$, a plasma current of $I_p = 1\,\text{MA}$ and a safety factor of $q_{95} = 4.4$. The electron density was gradually increasing between $2.5 - 3.5 \cdot 10^{19}\,\text{m}^{-3}$, which is 25-30 % of the Greenwald limit $\bar{n}_{\text{GW}}$. The geometry of the NBI sources at AUG is depicted in figure 3. The most radial beam Q4 has an inclination of 72° with respect to the
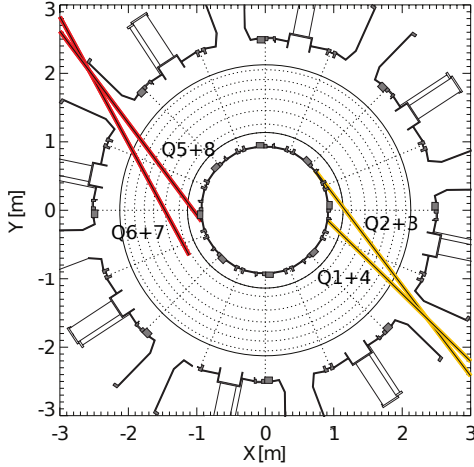
Figure 3. Top view of NBI sources Q1-Q8 in AUG is illustrating a relatively small difference between the most radial on-axis beam Q3 and the tangential on-axis beams Q3 and Q8.

magnetic axis, while the most tangential on-axis beam Q3 has an inclination of 58°. The last on-axis beam Q8 with an inclination angle of 60° has 40% lower torque input due to a higher acceleration voltage. The NBI heating starts with the source Q3 (1.5-3 s), followed by the source Q4 (3-4.5 s) and the source Q8 (4.5-6 s). The difference in the beam geometry between Q3 and Q4 causes a reduction of the torque. Therefore, the core deuterium Mach number decreases from $M_D = 0.32$ in the Q3 phase to $M_D = 0.20$ in the Q4 phase.

The fast particle distribution is modeled by the NUBEAM code in TRANSP, which calculates the time evolution of the fast particle density, and the perpendicular and parallel pressure. Moreover, at a few selected time-points, the complete particle distribution may be extracted. The NUBEAM simulation was calculated with $2 \cdot 10^5$ particle clusters, 40 radial bins and 10 ms time resolution. The redistribution of the fast particles by sawtooth crashes was included via the Kadomtsev model. The fast particle fraction reached up to 30% in the plasma center at the beginning of the Q3 phase (figure 4a) and it decreased to 12% during the Q4 and Q8 phase due to the increase in the electron density. The temperature anisotropy (figure 4b) in the Q3 phase was almost negligible, while during the phase with the radial beam Q4, the anisotropy increased to $T_\perp/T_\parallel \approx 2$. Later in the Q8 phase it dropped again to $T_\perp/T_\parallel \approx 1.4$. As a consistency check, the neutron rate is investigated in figure 4c. It depends mostly on the fast particle density and energy. We have normalized the number of the measured neutrons to the TRANSP results in the Q3 phase, because the absolute calibration for the neutron spectrometer [46] is unavailable. In the Q4 phase, which was also with a 60 keV NBI source, the calculated neutron rate corresponds to the measured rate, however, in the later phase using Q8, i.e. a 93 keV beam, the

rate was over-estimated by 30% which could imply an over-estimation of the fast particle density modeled by TRANSP. Nevertheless, the most important phases for this study are these with the beams Q3 and Q4 which mutually agree.
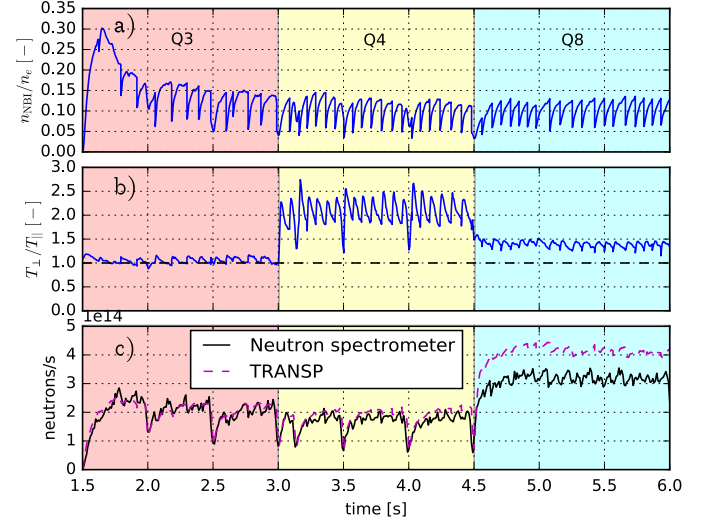

Figure 4. Temporal evolution of on-axis a) fast particles fraction n_{NBI}/n_e, b) temperature anisotropy $T_\perp/T_\parallel$ and c) total neutron flux as calculated by TRANSP for the discharge #32566, compared with neutron spectrometer measurement [46].

The two-dimensional profiles of the fast NBI ion density is obtained by integration of the distribution function over energy and pitch coordinates for each heating phase are shown in figure 5. The most significant LFS fast ions localization is driven by the Q4 beam due to the larger fast particle pressure anisotropy. The fast ions asymmetry is weak in case of Q3 and Q8 beams, because the asymmetry from the trapped and passing ions is mostly mutually canceled and only a subtle LFS surplus remains.
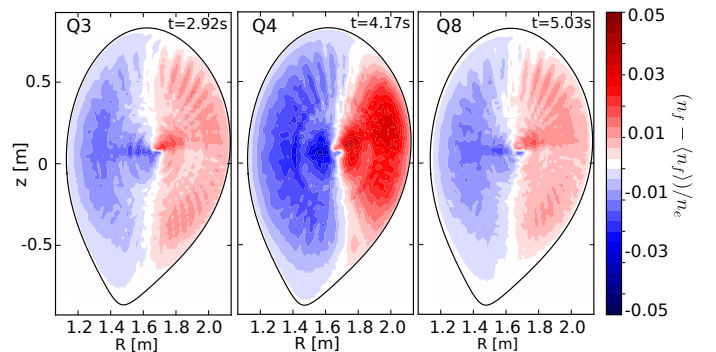

Figure 5. Background subtracted fast particle fraction calculated by the Monte Carlo model NUBEAM for each NBI heating phase.

The temporal evolution of the measured SXR asymmetry at $\rho_{pol} = 0.2$ is depicted by a green line in figure 6. In the Q3 phase, the asymmetry grows up to $\delta_{\mathrm{SXR}} \approx 0.6$. After switching to the radial beam Q4,

the asymmetry decreases to approximately $\delta \approx 0$, while large positive jumps occur just after the sawtooth crashes. In the last phase using Q8, the asymmetry increases to $\delta_{\mathrm{SXR}} \approx 0.2$.

The centrifugal model based on the formula (5) and including correction 13 for low-Z ions, explains well the Q3 phase, as is demonstarted via the red time-trace in figure 6. However, during the Q4 and the Q8 phases the CF model overestimates the experimental asymmetry, indicating the presence of another force affecting the W ions.

In order to calculate the temporal evolution of the fast ions driven asymmetry, the 2D profiles of n_{NBI}/n_e (figure 5) were rescaled by the flux surface averaged profile of fast ions density which is available for each time point of the TRANSP simulation. The combination of the electrostatic force (EF) and the CF asymmetry shown by the blue line in figure 6 was obtained by inserting the n_{NBI}/n_e profile to the approximation for electrostatic asymmetry (9). An excellent match is present in all three heating phases. In the Q4 phase, the asymmetry δ_{SXR} was reduced by 0.3 with respect to the CF model and the temporal evolution of the model even follows the spikes after sawtooth crashes which are caused by a rapid redistribution of the fast ions [47]. In both Q3 and Q8 phases, the asymmetry decreased by 0.15 with respect to the CF model. However, the relative change is twice as large for Q8 due to the lower torque input and thus a weaker centrifugal asymmetry.
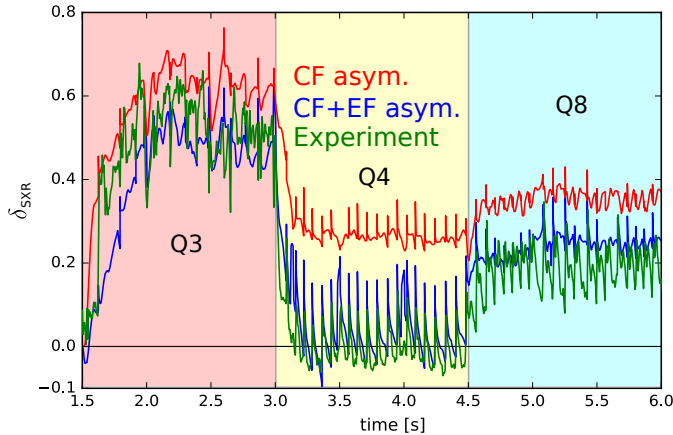

Figure 6. Time-trace of the poloidal asymmetry of SXR radiation in discharge #32566 at $\rho_{\mathrm{pol}} = 0.2$ (green) compared to the centrifugal model (red) and the model including electrostatic force from fast NBI particles (blue).

In conclusion, the electrostatic force from the fast NBI ions is a fundamental component of the parallel force balance of high-Z impurities in low-density NBI heated discharges in AUG. Moreover, the experimental scenario presented in this section provides optimal conditions to study the effects of such an asymmetry on the radial impurity transport, because only minor changes in the plasma parameters were observed despite the asymmetry

change from $\delta \approx 0.6$ in the Q3 phase to $\delta \approx 0$ in the Q4 phase.

5. Asymmetry driven enhancement of the radial impurity transport

Since the tungsten asymmetries are driven by heating sources like NBI or ICRF, large changes in the asymmetry are usually associated with a significant change in the heating, kinetic profiles, and MHD activity. Therefore, a proper experimental validation of the asymmetry enhanced neoclassical transport is challenging. However, it was demonstrated in the previous section that under optimal conditions a small variation in the inclination of the NBI beam can cause a massive reduction of the poloidal asymmetry. Moreover, the neoclassical transport has to be investigated in the very core of the plasma, in order to avoid the turbulent contributions to the impurity flux [26].

For the transport analysis the discharge #32324, similar to the previously analyzed #32566 is selected. The main difference with respect to #32566, is presence of the Q3 and Q4 heating phases only and a smaller variation in the sawtooth frequency. The kinetic profiles in both phases are depicted in figure 7. During the whole discharge, a regular sawtooth activities with an average period of $100\,\mathrm{ms}$ in the Q3 phase, and a period of $80\,\mathrm{ms}$ in the Q4 phase are present. The inversion radius is at $\rho_{\mathrm{tor}} = 0.26$ for both phases. The kinetic profiles are determined shortly before the sawtooth crashes and averaged over all sawteeth in the given heating phase. A small drop in the ion and electron temperature (see figure 7a) is caused by an increased electron density in the Q4 phase. Furthermore, the ion heat transport coefficient calculated from power balance χ_i^{PB} and its neoclassical value from NEO χ_i^{neo} (figure 7d) are unaffected by the beam switching, indicating a minor change in the anomalous heat transport. The tungsten density (figure 7e) is evaluated from a tomographic inverted SXR emissivity profile via SXR cooling factors [48]. The W profile develops a pronounced peaking in the buildup phase of the sawtooth which flattens after every crash, reducing the core W density by two orders of magnitude. The W profiles before the crash have an identical shape in both phases, however the W density exhibits a $30\,\%$ lower value in the Q4 phase. Finally, figure 7f) illustrates a dramatic change in the poloidal asymmetry which occurred after the transition between the Q3 and the Q4 phase.

The W transport coefficients, i.e. the diffusion coefficient D and the drift coefficient v/D, are evaluated for each sawtooth cycle by the least-squares (LSQ) optimization method following the approach described in [49]. In order to find D and v/D compatible with the experiment, these coefficients need to be modified until a solution of the transport equation for $n_{\mathrm{W}}(\rho, t)$ matching the measurements is found. The initial condition for the
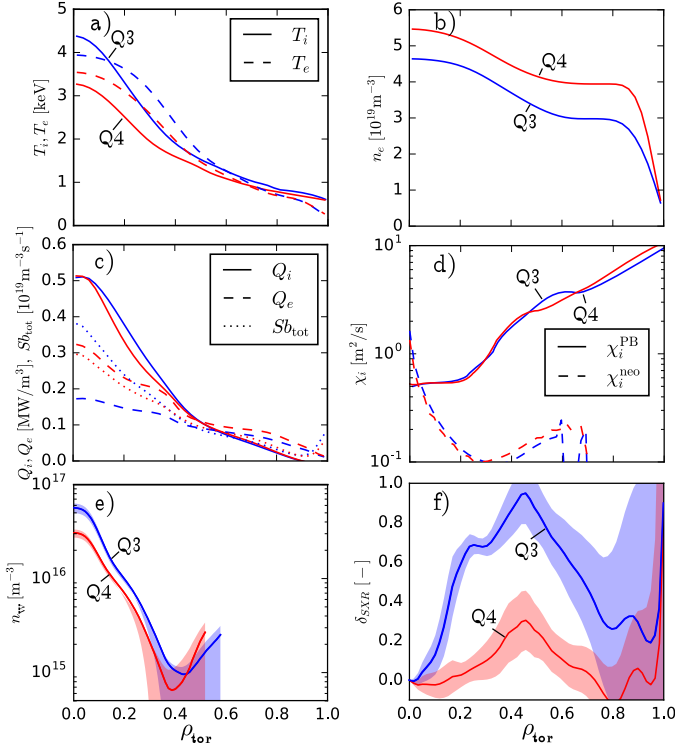
Figure 7. The profiles of basic plasma quantities in discharge #32324 for the Q3 heated phase (blue) and the Q4 heated phase (red): a) fit of a ion and electron temperature, b) fit of the electron density, c) the ion (full line) and electron (dashed line) heating profile and particle source (dotted line) from TRANSP, d) the ion diffusion coefficient from power balance (full line) and the neoclassical value (dashed line) e) tungsten density before the crash, f) measured poloidal asymmetry profile from SXR.

solution is defined by the density profile shortly after the sawtooth crash, while the measured impurity density at $\rho_{tor} = 0.3$ served as a radial boundary constraint.

Results of the fitting procedure are illustrated for a single crash during the Q3 and the Q4 phases in figure 8. The initial phase of the sawtooth cycle affected by the crash post-cursor and the final phase distorted by the crash precursor were removed from the analysis (figure 8a-b), because these modes were causing an additional outward impurity flux. Except these regions, an excellent match with the temporal evolution of the W density was found. The diffusion coefficient D in the Q3 phase, determining the magnitude of the neoclassical flux, significantly exceeds the value in the Q4 phase. The drift coefficients v/D are almost equal in both phases. The tungsten density in the Q3 phase was close to saturation, which is indicated by $v/D \approx L_{\langle n_z \rangle}^{-1}$ for $\rho_{tor} < 0.1$ as a dashed line in figure 8e-f. However, in the Q4 phase, the normalized gradient $L_{\langle n_z \rangle}^{-1}$ was almost twice lower than v/D in Q3 phase.

The experimentally measured transport coefficient were compared with the NEO model in figure 9. The comparison was evaluated at $\rho_{tor} = 0.12$ ($\varepsilon = 0.04$), close to the minimum in the v/D coefficient. For the NEO
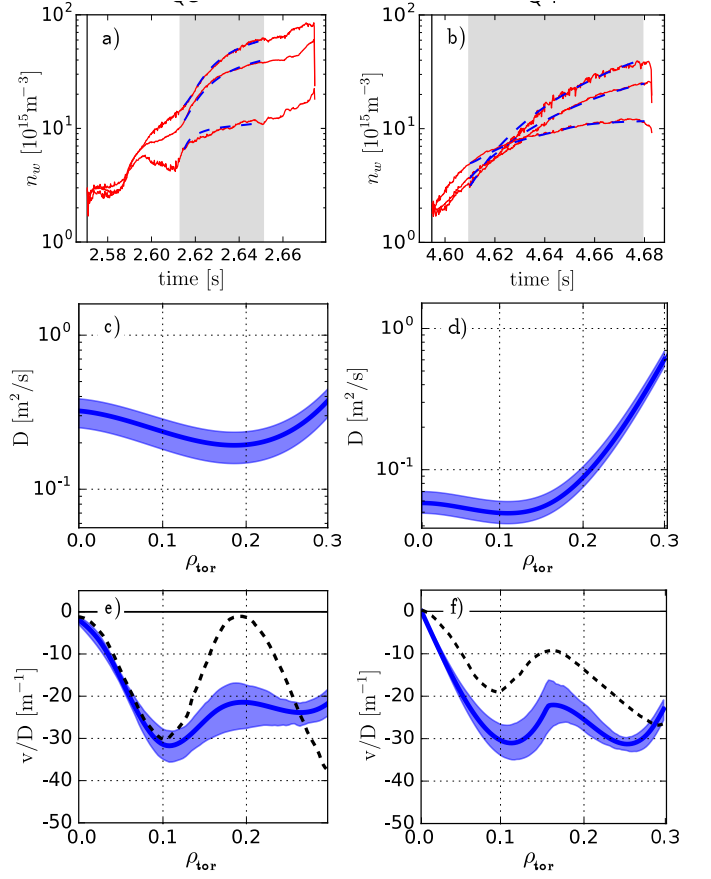

Figure 8. Transport coefficients estimated from the discharge #32324. The plots a,c,e) describe a sawtooth at 2.6 s and b,d,f) represent profiles for a sawtooth at 4.6 s. The shaded area in plots a-b) indicates the region selected for the transport analysis, the red lines show the measured W densities at $\rho_{tor} = 0$, 0.15, 0.3 m and the blue dashed line corresponds to fits by the LSQ method. The diffusion coefficient D is depicted in c-d) and the drift coefficient v/D in e-f). The black dashed line corresponds to $L_{\langle n_z \rangle}^{-1}$ evaluated just before the crash.

modeling, the kinetic profiles just prior to a sawtooth crash and averaged over several sawtooths cycles were used, and the asymmetry was varied in the range $\delta = -0.15$ to 0.4. The neoclassical value of D_W increased from $0.04 \, \text{m}^2/\text{s}$ at zero asymmetry to $0.7 \, \text{m}^2/\text{s}$ at $\delta = 0.25$. In the Q4 phase (red), the measured D_W matches well the neoclassical prediction. However, during the phase with parallel Q3 beam (blue), the NEO modeling overestimates the measurement D by a factor of 2-4, i.e. the timescales of the transport process should be 2-4× faster. Since the impurity density was already equilibrated before the crash, one can expect that the temporal dynamic of the impurity flux was affected by a slower peaking in the background profiles of n_i and T_i. Given the fact, that constant transport coefficients were assumed in the LSQ method, the measured D_W must by considered as a lower estimate for the actual neoclassical D_W^{neo}.

The neoclassical coefficient v/D (figure 8b) exhibits

only a limited variation with the W asymmetry. A small structure observed for $\delta < 0.04$ is caused by a drop in T_i screening (cf. 2b). This trend was confirmed by the experimental values of v/D, which stay unchanged within the uncertainties. A significant v/D variation should appear in discharges without n_i peaking for negative values of the asymmetry, where the T_i screening is significantly reduced. Such conditions occur when a LFS ICRF heating is used [10]. We leave confirmation of the neoclassical theory for the case with $\delta < 0$ for future work.
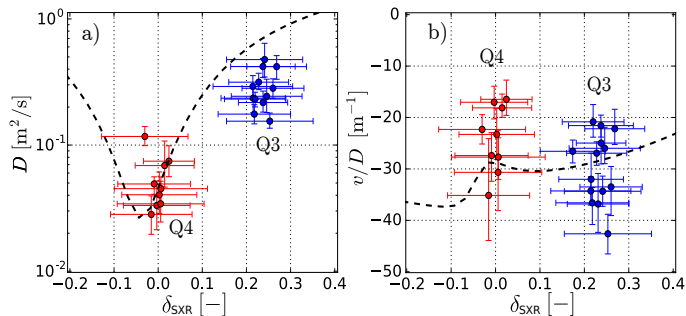

Figure 9. The neoclassical value of the transport coefficient (dashed lines) for the discharge #32324 at $\rho_{\text{tor}} = 0.12$ compared with the experimentally measured values (dots) in the Q3 phase (blue) and the Q4 phase (red) for the diffusion coefficient D a) and the drift coefficient v/D b).

6. Conclusion

In the present work, the parallel transport theory of the NBI heated discharges in AUG is investigated. A fast plasma rotation driven by a large torque input from NBI, results in a significant centrifugal force, trapping of the tungsten ions on the outboard side of the flux surfaces. Additionally, the non-thermal population of the fast NBI ions produces a perturbation in the poloidal electrostatic potential, which also affects highly charged tungsten ions. The variation in the poloidal tungsten profile was investigated using high-quality tomographic reconstructions of soft X-ray radiation, dominated by a tungsten contribution. Excellent match with the measured poloidal asymmetry was achieved when the fast particles distribution was modeled by a guiding orbit following Monte Carlo code NUBEAM. The strongest impact of the fast particles was observed for the most radial beam, where the centrifugal asymmetry is canceled by the electrostatic force from these ions.

The dramatic change in the poloidal asymmetry associated with the switching between parallel and radial beams, together with minor changes in the kinetic profiles, provides ideal conditions for the tungsten transport study. Tungsten transport coefficients were calculated by a least squares minimization of the difference between the measured W density profile from SXR and solution of the transport equation. The measured

diffusion coefficient, also determining the magnitude of the neoclassical transport, decreased five times, when the poloidal asymmetry was reduced by the switching. While in the weak asymmetry case the diffusion coefficient matches neoclassical value from NEO, D_W in the high asymmetry case is 2-4× less than NEO prediction. This could be an effect of the comparable timescale in the variation of the bulk ion profiles and W ions density during a sawtooth cycle, resulting in underestimated timescale of the W density equilibration. In the case of low asymmetry and thus a longer equilibration time is this effect negligible. Drift coefficient v/D describing W density peaking, is almost unaffected by the beam switching. This is in agreement with a neoclassical model, which is predicting only a minor changes in T_i screening. Further experiments with additional ICRF heating may be able to probe also negative asymmetry branch of neoclassical transport, where a substantial reduction in T_i screening and increase of D_W is expected.

References

[1] T Putterich, E Fable, R Dux, R Neu, MG O'Mullane, and R Wenninger. Impurity limits in a reactor grade fusion device. In *42nd EPS Conference on Plasma Physics*. European Physical Society, 2015.
[2] R Neu, R Dux, A Kallenbach, T Putterich, M Balden, JC Fuchs, A Herrmann, CF Maggi, M O'Mullane, R Pugno, et al. Tungsten: an option for divertor and main chamber plasma facing components in future fusion devices. *Nucl. Fusion*, 45(3):209, 2005.
[3] FL Hinton and SK Wong. Neoclassical ion transport in rotating axisymmetric plasmas. *Physics of Fluids (1958-1988)*, 28(10):3082–3098, 1985.
[4] SK Wong. Transport of impure plasma with arbitrary toroidal rotation. *Physics of Fluids (1958-1988)*, 30(3):818–829, 1987.
[5] K Indireshkumar and WM Stacey Jr. Effect of a poloidal electric field on neoclassical transport in a multispecies tokamak plasma. *Physics of Fluids B: Plasma Physics*, 5(6):1850–1868, 1993.
[6] J.A. Wesson. Poloidal distribution of impurities in a rotating tokamak plasma. *Nucl. Fusion*, 37(5):577, 1997.
[7] CS Chang and RW Harvey. Generation of poloidal electric field in a neutral-beam heated tokamak. *Nucl. Fusion*, 23(7):935, 1983.
[8] W Choe, CS Chang, and M Ono. Temperature anisotropy in a cyclotron resonance heated tokamak plasma and the generation of poloidal electric field. *Physics of Plasmas (1994-present)*, 2(6):2044–2054, 1995.
[9] L.C. Ingesson, H. Chen, P. Helander, and M.J. Mantsinen. Comparison of basis functions in soft X-ray tomography

and observation of poloidal asymmetries in impurity density. *Plasma Phys. Controlled Fusion*, 42(2):161, 2000.

[10] M.L. Reinke, I.H. Hutchinson, J.E. Rice, N.T. Howard, A. Bader, S. Wukitch, Y. Lin, D.C. Pace, A. Hubbard, J.W. Hughes, et al. Poloidal variation of high-Z impurity density due to hydrogen minority ion cyclotron resonance heating on Alcator C-Mod. *Plasma Phys. Controlled Fusion*, 54(4):045004, 2012.

[11] SK Wong. Modification of pfirsch–schlüter transport by poloidally asymmetric sources. *The Physics of Fluids*, 21(2):299–300, 1978.

[12] CS Chang. Enhancement of neoclassical transport coefficients by a poloidal electric field in tokamaks. *The Physics of fluids*, 26(8):2140–2149, 1983.

[13] W Feneberg. Neoclassical impurity transport in the presence of toroidal and poloidal rotation. *Nuclear Fusion*, 29(7):1117, 1989.

[14] P Helander. Neoclassical transport in a rotating impure plasma. *Physics of Plasmas (1994-present)*, 5(4):1209–1211, 1998.

[15] M Romanelli and M Ottaviani. Effects of density asymmetries on heavy impurity transport in a rotating tokamak plasma. *Plasma Phys. Controlled Fusion*, 40(10):1767, 1998.

[16] EA Belli, J Candy, and C Angioni. Pfirsch– Schluter neoclassical heavy impurity transport in a rotating plasma. *Plasma Phys. Controlled Fusion*, 56(12):124002, 2014.

[17] T Fulop and P Helander. Nonlinear neoclassical transport in a rotating impure plasma with large gradients. *Physics of Plasmas (1994-present)*, 6(8):3066–3075, 1999.

[18] C Angioni and P Helander. Neoclassical transport of heavy impurities with poloidally asymmetric density distribution in tokamaks. *Plasma Phys. Controlled Fusion*, 56(12):124001, 2014.

[19] K.L. Wong, Cheng C.Z., B.C. Stratton, and A Ramsey. In *Proceedings of the 14rd EPS Conference on Plasma Physics*. European Physical Society (EPS), 1987.

[20] KL Wong and CZ Cheng. Orbit effects on impurity transport in a rotating tokamak plasma. *Physics of Fluids B: Plasma Physics*, 1(3):545–554, 1989.

[21] KG McClements and RJ McKay. The orbital dynamics and collisional transport of trace massive impurity ions in rotating tokamaks. *Plasma Phys. Controlled Fusion*, 51(11):115009, 2009.

[22] T Nakano, N Asakura, H Kubo, J Yanagibayashi, and Y Ueda. Tungsten accumulation in H-mode plasmas of JT-60U. *Nucl. Fusion*, 49(11):115024, 2009.

[23] K Hoshino, T Takizuka, and T Nakano. Accumulation process of high-z impurity in toroidal rotating tokamak plasma. *Contributions to Plasma Physics*, 50(3-5):386–391, 2010.

[24] T Nakano et al. Tungsten transport and accumulation in JT-60U. *Journal of Nuclear Materials*, 415(1):S327–S333, 2011.

[25] C Angioni, P Mantica, T Putterich, M Valisa, M Baruzzo, EA Belli, P Belo, FJ Casson, C Challis, P Drewelow, et al. Tungsten transport in JET H-mode plasmas in hybrid scenario, experimental observations and modelling. *Nucl. Fusion*, 54(8):083028, 2014.

[26] C Angioni, FJ Casson, P Mantica, T Pütterich, M Valisa, EA Belli, R Bilato, C Giroud, and P Helander. The impact of poloidal asymmetries on tungsten transport in the core of jet h-mode plasmas. *Physics of Plasmas*, 22(5):055902, 2015.

[27] FJ Casson, C Angioni, EA Belli, R Bilato, P Mantica, T Odstrcil, M Valisa, L Garzotti, C Giroud, J Hobirk, et al. Theoretical description of heavy impurity transport and its application to the modelling of tungsten in jet and asdex upgrade. *Plasma Phys. Controlled Fusion*, 57(1):014031, 2015.

[28] EA Belli and J Candy. Kinetic calculation of neoclassical transport including self-consistent electron and impurity dynamics. *Plasma Phys. Controlled Fusion*, 50(9):095010, 2008.

[29] EA Belli and J Candy. An eulerian method for the solution of the multi-species drift-kinetic equation. *Plasma Physics and Controlled Fusion*, 51(7):075018, 2009.

[30] AG Peeters, Y Camenen, F James Casson, WA Hornsby, AP Snodin, D Strintzi, and Gabor Szepesi. The nonlinear gyro-kinetic flux tube code GKW. *Computer Physics Communications*, 180(12):2650–2672, 2009.

[31] FJ Casson, AG Peeters, C Angioni, Y Camenen, WA Hornsby, AP Snodin, and G Szepesi. Gyrokinetic simulations including the centrifugal force in a rotating tokamak plasma. *Physics of Plasmas (1994-present)*, 17(10):102305, 2010.

[32] Per Helander and Dieter J Sigmar. *Collisional transport in magnetized plasmas*, volume 4. Cambridge University Press, 2005.

[33] M.L. Reinke, J.E. Rice, I.H. Hutchinson, M. Greenwald, N.T. Howard, J.W. Hughes, J. Irby, Y. Podpaly, J.L. Terry, and A. White. Non-neoclassical up/down asymmetry of impurity emission on Alcator C-Mod. *Nucl. Fusion*, 53(4):043006, 2013.

[34] S. Suckewer, E. Hinnov, and J. Schivell. Rapid scanning of spatial distribution of spectral line intensities in plt tokamak. Technical report, Princeton Plasma Physics Lab, 1978., 1978. Technical Report PPPL-1430.

[35] A Lebschy, RM McDermott, B Geiger, M Cavedon, MG Dunne, R Dux, R Fischer, E Viezzer, ASDEX Upgrade Team, et al. Indirect measurement of the poloidal rotation in the core of asdex upgrade plasmas with charge exchange recombination spectroscopy. In *42nd EPS Conference on Plasma Physics*. European Physical Society, 2015.

[36] ML Reinke, IH Hutchinson, JE Rice, M Greenwald, NT Howard, A Hubbard, JW Hughes, JL Terry, and SM Wolfe. Parallel transport studies of high-z impurities in the core of Alcator C-Mod plasmas. 2013.

[37] R. Bilato, T. Odstrcil, F.J. Casson, C. Angioni, M. Brambilla, Ye.O. Kazakov, and E. Poli. The impact of the ion-cyclotron-resonance location on the poloidal asymmetries of impurity density in an icrf-heated rotating plasma. *Nucl. Fusion*, 57(5):056020, 2017.

[38] A Pankin, D McCune, R Andre, G Bateman, and A Kritz. The tokamak Monte Carlo fast ion module NUBEAM in the national transport code collaboration library. *Computer Physics Communications*, 159(3):157–184, 2004.

[39] RO Dendy, RJ Hastie, KG McClements, and TJ Martin. A model for ideal m= 1 internal kink stabilization by minority ion cyclotron resonant heating. *Physics of Plasmas (1994-present)*, 2(5):1623–1636, 1995.

[40] JP Graves, S Coda, WA Cooper, and L-G Eriksson. Modelling iccd experiments for sawtooth control in jet. In *Theory of Fusion Plasmas*, number CRPP-CONF-2006-093, 2006.

[41] T Odstrcil, T Putterich, R Bilato, M Weiland, D Mazon, A Gude, and ASDEX Upgrade Team. Investigation the fast particle velocity space by poloidal asymmetries of heavy ions. In *43nd EPS Conference on Plasma Physics*. European Physical Society, 2016.

[42] E Viezzer, E Fable, T Putterich, A Bergmann, M Cavedon, R Dux, RM McDermott, C Angioni, RM Churchill, MG Dunne, et al. Collisionality dependence of edge rotation and in–out impurity asymmetries in ASDEX Upgrade H-mode plasmas. *Nucl. Fusion*, 55(12):123002, 2015.

[43] V. Igochine, A. Gude, et al. Hotlink based soft X-ray diagnostic on ASDEX Upgrade (IPP 1/338). Technical report, Max-Planck-Institut fur Plasmaphysik, 2010.

[44] T Odstrcil, T Putterich, M Odstrcil, A Gude, V Igochine, and U Stroth. Optimized tomography methods for plasma emissivity reconstruction at the ASDEX Upgrade tokamak. *Rev. Sci. Instrum.*, 87(12):123505, 2016.

[45] J. DeLucia, S.C. Jardin, and A.M.M. Todd. An iterative metric method for solving the inverse tokamak equilibrium problem. *Journal of Computational Physics*, 37(2):183–204, 1980.

[46] G Tardini, A Zimbal, B Esposito, F Gagnon-Moisan, D Marocco, R Neu, H Schuhmacher, et al. First

neutron spectrometry measurements in the ASDEX Upgrade tokamak. *Journal of Instrumentation*, 7(03):C03004, 2012.

[47] M Weiland, B Geiger, Asger Schou Jacobsen, M Reich, Mirko Salewski, T Odstrcil, et al. Enhancement of the fida diagnostic at ASDEX Upgrade for velocity space tomography. *Plasma Phys. Controlled Fusion*, 58(2):025012, 2016.

[48] T Pütterich, R Dux, M Beurskens, V Bobkov, S Brezinsek, J Bucalossi, JW Coenen, I Coffey, A Czarnecka, C Giroud, et al. Tungsten screening and impurity control in jet. In *Proceedings of 24th IAEA Fusion Energy Conference (San Diego, USA, 2012), pp. EX/P3–15*, 2012.

[49] R Dux, A Peeters, A Gude, A Kallenbach, R Neu, and ASDEX Upgrade Team. Z dependence of the core impurity transport in ASDEX Upgrade H-mode discharges. *Nucl. Fusion*, 39(11):1509, 1999.